PHYSICAL REVIEW E VOLUME 53, NUMBER 2 FEBRUARY 1996

Steady state hydrodynamics of a lattice Boltzmann immiscible lattice gas

I. Halliday[1] and C. M. Care[2]
[1]*Division of Applied Physics, Sheffield Hallam University, Pond Street, Sheffield S1 1WB, United Kingdom*
[2]*Materials Research Institute, Sheffield Hallam University, Pond Street, Sheffield S1 1WB, United Kingdom*

(Received 17 April 1995; revised manuscript received 24 July 1995)

We report results from a simulation that assesses steady state hydrodynamics of two-phase lattice gas fluids by considering isolated fluid drops that are suspended in an immiscible fluid of identical viscosity. Gunstensen's method of incorporating phase segregation between different species of colored densities [(A.K. Gunstensen *et al.*, Phys. Rev. A **43**, 4320 (1991)] is combined with Kingdon's recent nonlinear, nonlocal lattice Boltzmann equation [R. Kingdon, J. Phys. A **25**, 3559 (1992)], which facilitates meaningful observations of lattice gas interfacial hydrodynamics. After the approach to a steady flow state has been assessed, the deformation of a suspended fluid drop, its angle of orientation to the shear flow, and the relationship between these quantities are extracted from simulations over a range of shear rates and interfacial tensions. Qualitative and quantitative comparison of these results with hydrodynamic theory shows further work to be necessary but worthwhile. Gunstensen's automaton phase segregation rule is also found to be responsible for inducing steady microscopic currents or microcurrents close to the inferface in a static flow. The influences of these microcurrents are briefly considered after Gunstensen [Ph.D. thesis, Massachusetts Institute of Technology, 1992 (unpublished)].

PACS number(s): 47.11.+j, 47.55.Dz, 47.55.Kf, 68.10.−m

I. INTRODUCTION

The lattice gas cellular automaton (LGCA) originally proposed by Frisch *et al.* in 1987 [1] is a lattice populated by monoenergetic particles propagating and undergoing momentum and number conserving collisions. Certain quantities extracted from simulations of this system, on a macroscopic scale, are close to bulk features of incompressible fluid flows and are, *ipso facto,* equivalent to solutions of the Navier-Stokes equation.

Additional degrees of freedom introduce into LGCA's interfaces between immiscible lattice fluids. Immiscible lattice gas automata (ILG's) first appeared in 1988 [2]. Rothman and Keller's ILG contains two species of particles, distinguished by their *color.* Rules for segregating species in collisions are all that is necessary to enrich the behavior of the LGCA to the extent that spontaneous phase separation arises. Previous work (Sec. II) demonstrates that ILG's behave, insofar as simulations of rest fluids are concerned, in a manner which admits of the association of a surface tension with the interface between separated colors. But whilst ILG's and their lattice Boltzmann equation (LBE) counterparts have been applied to the simulation of multiphase flows, some of which are quite complex [3], a fundamental question relating to the interfacial *hydrodynamics* remains open, possibly due to difficulties attending the attribution of velocities to particular phases in the interfacial region. For as is well known Gallilean-invariant hydrodynamic velocities derive from LGCA's only after rescaling lattice quantities and rescaling is obstructed by the presence of curved interfaces only one or two sites across (see Sec. II).

Occupying as they do a niche between molecular and traditional continuum hydrodynamics, ILG's are potentially useful. To be of any value as alternatives to CFD in multiphase complex flow applications, however, this aspect of ILG interfacial boundary behavior needs to be researched.

In [4] Kingdon reports a LBE algorithm which, whilst it models the usual collision process, takes into account isotropy and Gallilean invariance directly, requiring no rescaling to map lattice quantities onto solutions of the Navier-Stokes equation. A lattice Boltzmann ILG (LBILG) implementation based on the algorithm of [4] and the work of Gunstensen *et al.* in [3] will therefore address the problem of interface *location* by circumventing the necessity to rescale lattice quantities and hence facilitate evaluation of the model's steady state interfacial hydrodynamics—Sec. III.

To study steady state *dynamic* interfacial properties we therefore use a combination of the algorithms of Kingdon and Gunstensen *et al.* applied to the case of a small red fluid droplet suspended in a blue phase, to which different shear rates and interfacial tensions are applied in the manner considered in Secs. IV and V. The simulation's resulting steady state drop deformation behavior is presented in Sec. VI and discussed in Sec. VII, where semiquantitative comparisons with theory suggest further work is necessary.

ILG fluids, like real fluid media, are separated by transitional layers. For the latter, in the continuum regime, interface structure is unimportant. This cannot be said of ILG fluid interfaces, and, whilst here drop response to applied shears is the principal issue, we also report briefly upon measurements after Gunstensen [5], on steady *microcurrents,* induced at the interface by the segregation of colored species, for we shall argue in Secs. VII and VIII that their presence may have some bearing upon the capacity of a LBILG interface to recover "real world" hydrodynamic behavior.

1063-651X/96/53(2)/1602(11)/$06.00

II. CELLULAR AUTOMATON IMMISCIBLE LATTICE GAS HYDRODYNAMICS AND ITS LIMITATIONS

Rothman and Keller [2] augmented the original LGCA of Frisch *et al.* [1], populating it with particles of two colored species which inhabit the links $\mathbf{c}_i$, of a regular hexagonal lattice. Boolean quantities $r_j(\mathbf{x},t)$ $[b_j(\mathbf{x},t)]$ denote the number of red [blue] particles on the jth link beginning at position $\mathbf{x}$ and time step t. This diagram shows the link indexing convention used throughout the present report relative to the usual Cartesian axes.

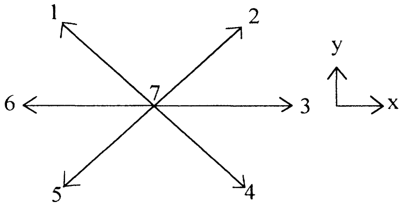

Node collisions now conserve individual color populations and, centrally, of all possible momentum conserving outputs from collisions between mixed species, the one selected maximizes the work done by site *color flux*

$$\mathbf{q}(\mathbf{x},t) \equiv \sum_i [r_i(\mathbf{x},t) - b_i(\mathbf{x},t)]\mathbf{c}_i \tag{2.1}$$

against a nonlocal approximation to the gradient in color difference, the *color field,*

$$\mathbf{f}(\mathbf{x},t) = \sum_{ij} [r_j(\mathbf{x}+\mathbf{c}_i,t) - b_j(\mathbf{x}+\mathbf{c}_i,t)]\mathbf{c}_i \ . \tag{2.2}$$

These additional rules bias postcollision particle distribution at sites of mixed color population, producing an accumulation of particles on lattice links perpendicular to an interface between red and blue lattice regions and a corresponding diminution on links parallel to that interface. Consequently the local ensemble average pressure tensor

$$\begin{aligned} P_{ab} &\equiv \sum_i \langle n_i(\mathbf{x},t)\rangle c_{ia} c_{ib} \ , \\ n_i(\mathbf{x},t) &\equiv r_i(\mathbf{x},t) + b_i(\mathbf{x},t) \ , \end{aligned} \tag{2.3}$$

becomes anisotropic and the two colored species spontaneously separate.

Such models of hydrodynamics unfortunately contain high levels of statistical noise. Whilst there is a growing realization that fluctuations are actually useful in adapting lattice gas techniques to the simulation of colloidal systems, large scale (parallel) ILG simulations after [2] have attributes (invisible on the time and spatial scales of the original simulation of Rothman and Keller) which restrict their practically for present purposes, namely, persistent oscillations in both shape and interior pressure [6]. Moreover, small scale circulations or microcurrents ([5], see Fig. 5, below) induced close to the interface are observed and clearly of interest. These, we argue in Sec. VII, are to be expected as a consequence of the particular means of color separation used by the Rothman-Keller (RK) rule and, like drop shape information, quantitative observation of microcurrent activity is hindered by the inherent noise. The significance of these considerations is, however, overshadowed by a more important limitation on the CA based ILG's, associated with rescaling.

Hydrodynamic velocity fields are recovered from the automaton only after the instantaneous *node* quantities $\sum_i n_i(\mathbf{x},t)$ and $\sum_i n_i(\mathbf{x},t)\mathbf{c}_i$ have first been ensemble averaged and then rescaled [1]. Denoting the ensemble average value of $n_i(\mathbf{x},t)$ by $N_i(\mathbf{x},t)$ (the link *density)* the lattice fluid site density and velocity are given by

$$\rho(\mathbf{x},t) \equiv \sum_i N_i(\mathbf{x},t) \ , \tag{2.4a}$$

$$\mathbf{v}(\mathbf{x},t) \equiv \frac{1}{\rho(\mathbf{x},t)} \sum_i N_i(\mathbf{x},t)\mathbf{c}_i \ . \tag{2.4b}$$

Subsequent *rescaling* (Ref. [1], section 7.2 onwards) maps quantities (2.4), respectively, onto incompressible hydrodynamic pressure and velocity. Rescaling involves spatial and temporal averaging over sublattices and consecutive time steps [1] and this clearly introduces ambiguities when applied near interfaces only a few sites thick. For, with small drops, interfacial curvature may be significant over the rescaling region, so difficulties arise in assigning velocities to particular automaton fluid phases. Such difficulties in defining meaningful interfacial velocity fields in the ILG automaton clearly present a problem, because target "real world" hydrodynamic interfacial boundary conditions concern continuity of stress contractions and velocity components (e.g., [7]), and these relate directly to the interfacial velocity field.

III. LATTICE BOLTZMANN IMMISCIBLE LATTICE GAS HYDRODYNAMICS

In this section we consider the established methods already in the literature which are combined to advantage in the present work, deferring until the next section the actual details of our simulations.

A LBILG approach to lattice gas hydrodynamics contains ensemble averaging, although not necessarily the rescaling of the automaton, and so overcomes the limitation of noise explicitly [1,8,9,6]. In place of the direct simulations of the CA a two-dimensional LBE uses a plain hexagonal lattice, whose links are populated not by particles but by the corresponding (continuous) densities $N_i(\mathbf{x},t)$. Analysis of the automaton algorithm shows [1,9] that, if at discrete times these densities are propagated and collided by adjusting them in a manner designed to be consistent with the number conserving automaton particle collisions, their values continue to represent ensemble average values of $n_i(\mathbf{x},t)$. Unfortunately the methods for colliding densities do not appear to have been compared or detailed consistently in the literature. Approaches based upon a linearized collision matrix (e.g., [9]), nonlinear analysis of automaton collisions [3], and nonlocal approaches [4] have been used.

Of the methods cited (i.e., [1,3,8]) the most recent and most clearly documented (two-dimensional) version is Kingdon's [4]. Whilst nonlocal (it utilizes velocity gradients in updating the densities) Kingdon's method incorporates Galilean invariance directly and explicitly recovers the mapping of quantities similar to (2.4) onto the incompressible Navier-Stokes equation without rescaling. An additional advantage of Kingdon's algorithm is that it allows parametrization of the simulated fluid shear viscosity. However, relying as it does on velocity gradients which must be calculated with reference to information from adjacent sites, Kingdon's scheme proves to be computationally inefficient compared with other local lattice Boltzmann schemes [10].

Interfaces are actually introduced into LBILG's by the use of colored *densities*. Red and blue densities, the average probabilities of finding a red or blue particle on link i at position $\mathbf{x}$ and time t, are written $R_i(\mathbf{x},t)$ and $B_i(\mathbf{x},t)$, with the overall density given by

$$N_i(\mathbf{x},t) \equiv R_i(\mathbf{x},t)+B_i(\mathbf{x},t) \ . \tag{3.1}$$

In modeling collision processes at a site, the $N_i(\mathbf{x},t)$ are adjusted with no reference to its color composition. It is clearly necessary to couple the lattice distribution of color to the distribution of mass, and so a means of allowing these quantities to interact is introduced.

Between the two colored species an interface is maintained in the LBILG in this work following a prescription first reported by Gunstensen *et al.* [3], which incorporates phenomenologically into a LBILG the color field biased, multicolored collisions of Rothman and Keller's CA scheme. A LBILG color field is a nonlocal approximation to the gradient of color difference generalized naturally from the automaton case (2.2):

$$\mathbf{f}(\mathbf{x},t)=\sum_{ij}[R_j(\mathbf{x}+\mathbf{c}_i,t)-B_j(\mathbf{x}+\mathbf{c}_i,t)]\mathbf{c}_i \ . \tag{3.2}$$

It is essential to incorporate an influence due to the color field similar to the bias its presence produces in an ILG *automaton.* On mixed nodes $\mathbf{f}(\mathbf{x},t)$ is used to perturb the $N_i(\mathbf{x},t)$ and Gunstensen *et al.* use a number and velocity conserving perturbation selected from a number of possibilities (see Sec. VII):

$$\Delta N_i(\mathbf{x},t)=\sigma|\mathbf{f}|\cos[2(\theta_f-\theta_i)] \ , \tag{3.3}$$

where θ_i denotes the angular orientation of the ith link and θ_f the continuous angular orientation of the color field $\mathbf{f}(\mathbf{x},t)$.

In summary, then, collision steps are performed using Kingdon's scheme [4], modified to contain red and blue species in a manner similar to that used by Gunstensen *et al.* [3]. Collided and perturbed densities are then allocated (conserved) color in such a way as to maximize the segregation of colored species, as explained in Sec. IV.

Collision updated, perturbed, and recolored densities are finally propagated along lattice links to the next lattice node, which completes a compound update step.

IV. SIMULATIONS OF STEADY STATE DEFORMED DROPS USING A LBILG

Details of our particular LBILG simulation are given here. As it is our aim to assess the steady state hydrodynamics of a single suspended drop, utilizing the fundamental work discussed in Sec. III, we consider to be relevant the postcollision allocation of color, the means by which flow is forced (boundary conditions), and the stability of observations.

A. Interfacial perturbation and allocation of color

In our algorithm, for the sake of simplicity, the factor $|\mathbf{f}|$ is omitted from the interfacial perturbation (3.3). From (2.3) and (3.3), increasing the parameter σ will increase local anisotropy in the pressure tensor, which, together with a color density segregation procedure, produces an interface between the two species. After adjusting the $N_i(\mathbf{x},t)$ to include both the effect of collision processes and the effect of an interface, the total red mass on a mixed site is assigned to densities in such a way as to optimize the red flux in the direction of the color field (and implicitly the blue flux in the opposite direction).

Attribution of color to achieve this requires a priority for red occupancy (1–7) to be associated with every link. In fact, it is necessary only to classify any given color field into one of 12 30° intervals in order to obtain this hierarchy, not 36 as reported previously in [2]. Accordingly, the link given the maximum red mass is that subtending the smallest angle to the color field direction. All red mass on a mixed site is assigned in this way, to links in descending priority until exhausted. Remaining capacity on links at the mixed site in question is thereafter designated blue. By this process we obtain that postcollision state which minimizes the local work $W(\mathbf{x},t)\equiv-\mathbf{f}(\mathbf{x},t)\cdot\mathbf{q}(\mathbf{x},t)$ done by the color flux [generalization of (2.1)] against the color field.

It is appropriate to emphasize here that the sequence of collision, perturbation, and finally propagation should be preserved. For if a collision step is performed immediately after some perturbation, that collision will alter the densities, overwhelming the effect of the preceding perturbation. This is particularly true of the method used to induce flow, since the LBILG used here with periodic boundaries applies perturbations to link densities at the edges of the lattice in order to generate the desired flow conditions. Note also that anisotropy in the pressure tensor is also the cause of interfacial microcurrents and both these effects are influenced through (3.3) by the value of the parameter σ, as first observed by Gunstensen in [5].

B. Forcing flow

In the simulations an approximate hydrodynamic shear field was obtained by imparting uniform velocity in the positive (negative) x direction at all points in a line at the bottom (top) of the simulated blue fluid. An appropriate forcing effect is accomplished in the LBILG by exploiting periodic boundary conditions and perturbing link densities. Because periodic boundary conditions are encountered, care should be exercised in ensuring that the correct perturbation is applied to the correct link. Thus, along a line of sites at the bottom of the lattice, a small constant increment is applied at every time to $N_5(\mathbf{x},t)$ and $N_2(\mathbf{x},t)$ (for link indexing, refer to the diagram on p. 1601). This perturbation is called a *force increment* F_{inc}

it acts to force flow at the site of application. Conversely, on these same sites, densities $N_1(\mathbf{x},t)$ and $N_4(\mathbf{x},t)$ are decremented by F_{inc}, the overall site density remaining constant. Periodic boundary conditions were in force all around, so perturbed densities on links 4 and 5 along the lattice bottom actually propagate around to the top of the lattice where they produce the correct forcing effect in the negative x direction. Because of this exploitation of periodic boundary conditions it is especially important that flow forcing perturbation be applied immediately before the propagation step.

Data were extracted only from closing configurations and, moreover, only from closing configurations in which the suspended drop was approximately central on the lattice, thus ensuring a symmetric exposure to the applied flow field. *Ipso facto* flow forcing perturbations were applied exclusively at pure blue sites.

The simple measures described above are sufficient to induce a shear field in a single phase fluid, the size of which is directly proportional to the size of the force increment used. The presence of a droplet will partially deflect the flow and the velocity field induced in the multiphase fluid is not a simple shear in the vicinity of the drop. However, at a distance from the drop one can expect an approximate shear flow. This simple observation provides the principle restriction upon the maximum size of a drop for a given lattice dimension.

Drops considered in these simulations posed a sufficiently small "obstruction" on a lattice of given size to allow for the development of a measurable shear in the *far field* of the flow (distant from the center of the drop). The simulated red drop size was determined by the requirement that, for all drop deformations encountered, steady state far field shear rates could be accurately recorded. The precise way in which shear rate $\dot{\gamma}$ was actually quantified is considered along with system size in more detail in Sec. V A.

C. Steady state values of simulation observables

The purpose of the work reported here was to assess hydrodynamics of the ILG in the steady state. Clearly, simulation responses should be constant when measured and it is therefore essential that the approach to a steady state be studied carefully.

Drop deformation, orientation, internal pressure, suspending blue fluid shear rate $\dot{\gamma}$, and the total instantaneous *work* defined by

$$W_0(t) \equiv -\sum_{\mathbf{x}} \mathbf{f}(\mathbf{x},t)\cdot\mathbf{q}(\mathbf{x},t) \tag{4.1}$$

were all defined and measured as a function of simulation time step. Only lattice configurations in which all of these quantities have settled to within 0.7% of their steady value were analyzed for drop response, which was assessed from data derived from its inertia tensor (see Sec. V C).

Internal pressure, deformation, and "total energy" defined through (4.1) were all recorded at each time step. The most flexible drop subject to the largest shear equilibrates in approximately 8000 time steps. All the data presented in Figs. 1–7 below are obtained from analyses of the final lattice state of flows evolved for 12 000 time steps. The data presented (for larger systems but smaller shear rate) were obtained from final lattice states after 10 000 time steps.

In order briefly to study scaling with R and σ of interfacial microcurrents the hexagonal symmetry of the *rest* simulation was exploited. Considering only a 60° segment of the drop centered on the bottom left of the lattice clearly expands the size of the simulatable system. Periodic boundary conditions which rotate through 60° the direction of motion of particles propagating off the left- (right-) hand edges of the lattice before they reenter at the *bottom (top)* facilitate simulations six times larger than those possible employing the more usual rectangular boundary conditions. In our case a range of drop radii up to 18 lattice units on effective lattices of $6\times25\times25$ sites was obtained from actual lattices of only 25×25 sites. Results shown in Figs. 8 and 9 below are, however, obtained from drops of radius 12 lattice units on larger lattices of 50×50 sites.

V. OBSERVED QUANTITIES AND PARAMETER RANGE CONSIDERATIONS

Applied shear rate $\dot{\gamma}$ (controlled by the simulation parameter F_{inc}) and the interfacial tension Σ (controlled by the simulation parameter σ) between the lattice fluids are the most appropriate simulation observables with which to parametrize the droplet response. *Ipso facto,* a means of defining and measuring these quantities should be defined but this process is bound up with considerations of system size. Moreover, it is appropriate, before discussing our selection of parameter range, to note that for all the simulations reported both fluids had the same shear viscosity of 0.02 and initial density of 1.4.

A. Macroscopic surface tension

The Laplace law, which relates Σ, the pressure difference across an interface Δp, and the principal interfacial radii of curvature [7] may, in two dimensions, be written

$$\Delta p = \frac{\Sigma}{R}\ , \tag{5.1}$$

where R is the drop radius. Taking R as the average distance from the center of mass of the drop to an interfacial site, Rothman and Keller [2] observed Laplace law behavior in ILG static droplets. Whilst the present LBILG is different from others in the literature it should certainly exhibit this static behavior. Moreover, a calibration of the parameter σ against macroscopic interfacial tension Σ is an aid in the sequel. For Kingdon's algorithm the hydrostatic pressure p is approximately $p=\rho/4$ so that the pressure difference across the interface may be obtained from appropriate differences between overall interior and exterior site densities.

B. Shear rate $\dot{\gamma}$

In multiphase simulations, near field flow is not simple shear. To measure $\dot{\gamma}$ it is first necessary to consider the problems attending its definition in the context of system size. Essentially, in order to quantify $\dot{\gamma}$ it is necessary to consider velocities at a distance from the drop sufficient for the flow to be regarded as a shear. This in turn makes it necessary to determine the largest possible measurable *deformed* drop which will admit of this approximation on a given size of lattice.

Clearly, the greatest possible vertical distance away from a centrally placed red drop is half the lattice width. An effective $\dot{\gamma}$, then, was defined by averaging velocity gradient $\partial v_x/\partial y$ at all sites within a narrow horizontal band of restricted depth, situated at both the top and bottom of the lattice, in what was taken to be the far field of the flow (see below). The velocity gradients were defined after [4] in terms of density gradients. In defining the averaging bands forced sites were excluded and at any averaging site the ratio of x to y velocity components was <0.1. A lattice velocity has dimensions of lattice spacing per unit time so the $\dot{\gamma}$ defined in this way as a lattice velocity gradient has dimensions of reciprocal time which is inconvenient for comparison with theory.

Obviously a velocity component in the y direction might be reduced by increasing the parameter σ or decreasing F_{inc} (to reduce drop deformation) or by reducing the radius of the undeformed drop. So for given lattice size a need to define and measure the $\dot{\gamma}$ defined above restricts the range of undeformed drop radius and that of the parameters σ and F_{inc}. The results of Figs. 1–7 in Sec. VI apply to a small drop of radius 7 lattice units which on a 32×32 lattice, by trial and error, was found to constrain σ and F_{inc} to lie within the approximate ranges $0.001<\sigma<0.01$ and $0<F_{\text{inc}}<0.008$.

C. Drop deformation and orientation

Throughout, the lab frame is taken to be coincident with the shear flow direction and as a simplification we regard the deformed drop shape as an ellipsoid, which assumption was tested by a grid search optimized fit of the perimeter to a rotated ellipsoid and found to be satisfactory.

Drop symmetry axes coincide with the principal axes of the inertia tensor with the smallest principal moment corresponding to the semimajor axis of the ellipsoid. Following the traditional procedures of simulation physics, the deformation of the drop was measured using an order parameter derived from a *traceless* inertia tensor. The center of mass of an established, deformed drop was located by considering moments about the origin of coordinates. Components $I_{ij}\equiv\sum m(r^2\delta_{ij}-x_ix_j)$ of the inertia tensor $\underline{I}$ were calculated [11]. An orthogonal transformation on $\underline{I}$ yields the drop's principal moments of inertia from the eigenvalues of the associated secular determinant and the *lab frame* orientations of the drop semimajor and semiminor axes were obtained from the direction cosines of the principal axes of $\underline{I}$. The *traceless* inertia tensor was evaluated from

$$\underline{I}-\tfrac{1}{2}\text{tr}(\underline{I})\underline{1}_{22}\ , \tag{5.2}$$

where $\underline{1}_{22}$ is the unit two-dimensional matrix. Diagonal elements of expression (5.2) are given by the *order parameter*

$$D\equiv\tfrac{1}{2}(I_x-I_y)\ , \tag{5.3}$$

where I_x and I_y are the principal moments corresponding to rotation about the "semiminor" and "semimajor" axes, respectively. The quantity D of course increases as droplet eccentricity increases and vanishes for a circular drop.

The angle at which the ellipsoidally deformed drop orientates itself, relative to the direction of the forced flow (taken to be the x axis), is parametrized by the angle subtended at the horizontal by the semimajor axis of the ellipse. This quantity, which also may be obtained from the inertia tensor of the drop, is denoted α.

For purposes of quantitative comparison with theory, using larger simulations, we introduce a second deformation parameter. a and b representing drop semimajor and semiminor axis lengths we define after [12],

$$D_C\equiv\frac{a-b}{a+b}\ . \tag{5.4}$$

Having identified the accessible range of simulation observables, care should be exercised in ensuring the stability of the final droplet configurations analyzed. This assurance can only be obtained from a study of the approach of the droplet to the deformed steady state.

The results of Figs. 8 and 9 below are used to make comparison with theory. They derive from drops of radius 12 on lattices of 50×50. $\sigma=0.001$ was selected so as to limit microcurrent activity (Secs. VI and VII) and, since Cox [12] considers as small drop deformations for $D_C\leq0.2$, a range of flow forcing parameter $0<F_{\text{inc}}<0.001$ consistent with this upper limit of D_C was used so as not to preclude comparison with the perturbation calculation [12]. Parametrization of the deformed drop shape is obstructed by lattice anisotropies at very small deformations (hence the need for increased system size) which result from very small shear rates, so it was necessary, having determined a, b, and α from an analysis of the inertial tensor (5.2), to grid-search optimize these observables using a least-squares fit to the interface.

Note that our angle α and that of Cox in [12] are defined with respect to different coordinate axes and so differ by $\pi/2$ rad.

D. Parametrization of interfacial microcurrents

We assess here only those aspects of interfacial microcurrents which impinge upon the behavior of the steady state dynamical properties of the interface. Microcurrent data were collected from a static simulation using the sectional periodic boundary discussed above (Sec. IV C). By normalizing the velocity field to the largest recorded velocity (always similarly located relative to the interface) and forming the inner product summation $\sum_{\mathbf{x}}\mathbf{v}(\mathbf{x},t)\cdot\mathbf{v}(\mathbf{x},t+1)$ it is possible to compare the velocity fields of different simulations with identical sizes. The velocity recorded as characteristic of the interfacial microcurrent was in each case the maximum flow velocity occurring close to the color boundary. This quantity was observed always to occur in approximately the same location *relative to the interface* and was measured for a range of σ and R (Figs. 5 and 6 below and Gunstensen [5]).

VI. RESULTS

For the part of the ranges of simulation parameters accessible (Sec. V B) we present measurements of D [defined by (5.3)] and α as functions of the blue fluid shear rate $\dot{\gamma}$ (which serve for qualitative and semiquantitative comparison with theory), measurements of microcurrent activity and, for quantitative comparison with theory, the variation of α with D_C [defined by (5.4)]. Whilst by the criteria outlined in Sec. V we give only a subset of our data, selection has been made purely for clarity of presentation and the trends in our data are entirely representative.

Figure 1 shows an example of the equilibration of simulation observables, each normalized to its relative steady state value, for simulation parameters $(\sigma,F_{\text{inc}})=(0.0002,0.0005)$ used in Figs. 1–7 below. Internal pressure is omitted from Fig. 1, since, for the example considered, it develops in less than 400 time steps to a steady value which appears constant and thereafter fluctuates by less than 0.07%. Figure 1 is also representative of the approach to the steady state exhibited by the larger systems considered in Figs. 8 and 9 below. Note that in this figure droplet deformation is measured by the ratio of the principal moments of the drop inertia tensor, not by D or D_c.

During the approach to the steady state the internal pressure converges most rapidly. W_0 and the deformation D appear to stabilize on a considerably longer time scale. From (4.1) it is clear that the surface energy W_0 must increase with interface length and once the value of internal pressure (red site density) is constant it follows from conservation of color that the volume of the drop is fixed. In all the cases recorded, α initially converges onto its steady state value more rapidly than both W_0 and D; however, in general all these observables appear to equilibrate asymptotically over approximately the same time but all three (W_0, D, and α) appear to be fixed only in the steady state, and it is possible that W_0 may be regarded as a function of state for the macroscopic deformed drop, sensitive to the shape of the latter.

Figure 2 shows the surface tension calculated from the Laplace law (5.1) as a function of the independent simulation parameter σ. Over the range used in these simulations there is a convincing linear relationship between the two quantities. Optimum straight line behavior is obtained with a gradient of 3.4689 and an ordinal intercept of 0.0002.

Figure 3 shows α, the angle subtended by the drop semimajor axis to the horizontal, as a function of $\dot{\gamma}$ and Fig. 4 the variation of deformation D with $\dot{\gamma}$. In both these figures $\dot{\gamma}$ was measured following the prescription discussed in the previous section and the values of Σ from the static calibration (Fig. 1) used to obtain the data series parametrizations used in Figs. 3 and 4.

In attempting to assess the implications of the information contained in Figs. 3 and 4 for the LBILG's macroscopic hydrodynamics, it is useful to consider that our applied shear flow field may be decomposed into a strain and a rotation, the axis of elongation in the component strain being oriented at 45° to the direction of flow [13,14]. For the surface tension dominated case of small deformation considered by Taylor [15], the drop will be stretched along a line inclined at 45° to the flow direction, into a spheroidal shape. Moreover, since the component strain is proportional to the applied shear rate, for small deformation one expects a linear relationship between D and $\dot{\gamma}$. Clearly this behavior will complicate as larger shear rates are applied and, affected by the flow's component rotation, α will vary—as the deformation increases the drop poses more of an "obstruction" and its

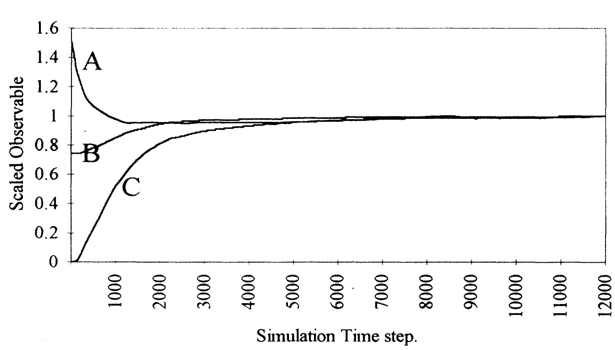

FIG. 1. Simulation observables in the approach to the steady state. Curve A shows the evolution of the drop orientation angle α (see Sec. VI), curve B the development of the ratio R of the inertia tensor principal moments, and curve C the total lattice work W_0. These data are not relevant to the results of Figs. 8 and 9 below.

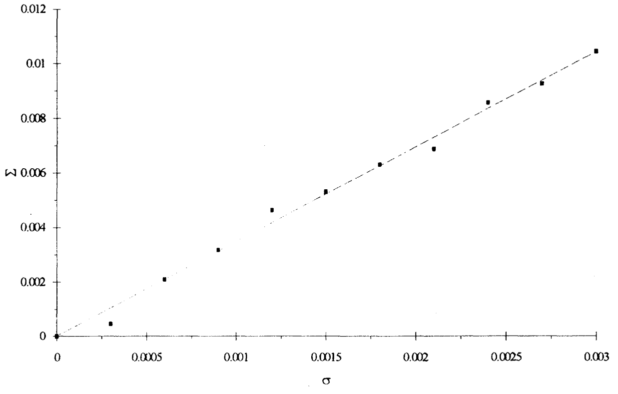

FIG. 2. Macroscopic surface tension Σ, obtained from Laplace's law, as a function of the simulation parameter σ. The solid line shows the least-squares fit to the data, the solid squares the actual data. The macroscopic surface tension Σ corresponding to the simulation parameter σ is used to parametrize the results of Figs. 3 and 4. Similar results were obtained for the data presented in Figs. 8 and 9 below.

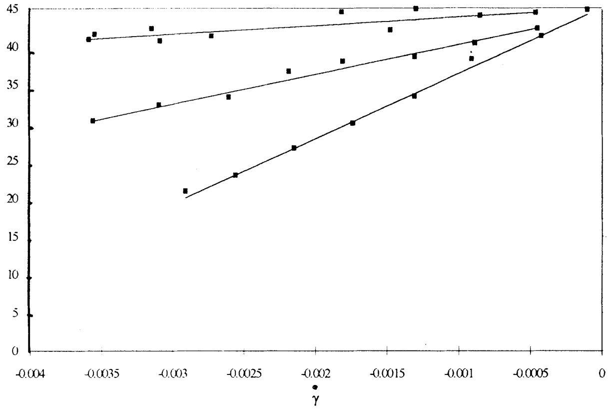

FIG. 3. The angular orientation of the drop, measured in degrees, shown as a function of applied blue fluid shear rate $\dot{\gamma}$. The solid lines are lines of least-squares fit to three data series each parametrized (upwards) by values of macroscopic surface tension (Σ) 1.04×10^{-3}, 2.08×10^{-3}, and 0.33×10^{-3}. Each data point corresponds to a simulation on an initially circular drop of radius 7 lattice units on a lattice of 35×35 sites, "equilibrated" for 12 000 time steps. The drop with the smallest interfacial tension is that which is most rotated by the external flow. In small shear fields all assumed ellipsoidal drops subtend an angle of 45° to the flow direction.

semimajor axis will orientate closer to the horizontal. In principle, α decreases with increasing $\dot{\gamma}$, but will tend to 45° in small applied shears. These trends are evident in our results of Fig. 3. At very small shears, the drop shape is affected by anisotropies introduced by the lattice, so that the assessed angular orientation α becomes inaccurate. However, extrapolation from larger shear rates shows α tending to 45°, in agreement with the three-dimensional analytical calculations of Taylor [15] and Cox [12]. The predictions of [12] are valid only for small deformation and unit applied shear rate. They are fully adapted to three dimensions; however, it may be shown that the linear relationship between deformation and $\dot{\gamma}$ and between α and $\dot{\gamma}$ predicted in [12] does remain valid in two dimensions. For practical purposes, the shear rates used to parametrize the results (Figs. 3 and 4) are perhaps unsatisfactory but a more quantitative comparison with theory may be made by considering the relationship between the parameters α and D, which is the content of Fig. 8, discussed below.

Figures 5 and 6 characterize the steady state microcurrents induced in the interfacial region of a static drop. Figure 5 depicts a *scaled* flow field in which velocities have first been normalized to the maximum microcurrent velocity $V_{\max}$ and then represented by arrows of three types (see the key to Fig. 5). As one might expect, the principal microcurrent activity is consistent with the symmetry of the lattice and (although obscured somewhat by the way in which the velocity field of Fig. 5 is drawn—see key) restricted in range to cells the maximum velocity in each of which occurs in equivalent positions in equivalent simulations. $V_{\max}$ may therefore be regarded as a meaningful measure of microcurrent activity. In Fig. 6, this quantity was recorded for identical drops over a range of the σ parameter [Fig. 6(a)] and for fixed σ over a range of drop radii [Fig. 6(b)]. Gunstensen

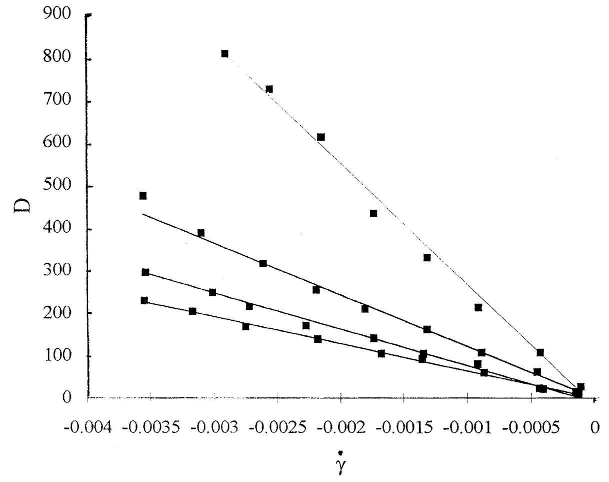

FIG. 4. Deformation of the drop, parametrized by D (Secs. V C and VI), as a function of blue fluid shear rate $\dot{\gamma}$. The solid lines are lines representing least-squares fits to four data series (solid squares) each parametrized (downwards) by values of macroscopic surface tension (Σ)1.04×10^{-3}, 2.08×10^{-3}, 0.33×10^{-3}, and 0.40×10^{-2}. See Fig. 3 caption for simulation details. The drop with the smallest interfacial tension is that which is most deformed by the external flow. In small shear fields all deformed drops tend to become circular.

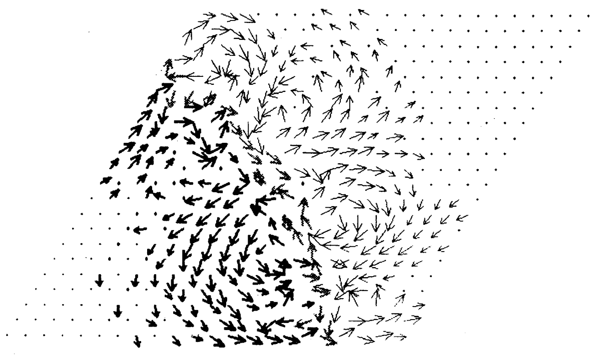

FIG. 5. Microcurrent activity for an unforced drop of fixed radius 18 lattice units, with surface tension parameter 0.0015 (see Fig. 2). This result was obtained using the hexagonal boundary conditions (discussed towards the end of Sec. IV). All velocity vectors' moduli v in this fully developed, steady state have first been normalized to the maximum value $V_{\max}$. Arrows represent flow at lattice nodes with more than 0.0001% color *impurity*. To emphasize the microcurrent pattern the circulations are represented by dots for lattice sites where $R\equiv v/V_{\max}$ is such that $0.005V_{\max}>R$, small vectors for $0.005V_{\max}<R<0.1V_{\max}$, and by large vectors for $0.1V_{\max}<R$. The qualitative features of the induced flow pattern were observed to vary little between simulations parametrized by different values of σ.

has already detailed the variation of microcurrent magnitude in [5]. To the best of our knowledge, however, this work has never been presented in the international literature. Figure 6(a) shows a linear correlation between σ and $V_{\max}$, which may be understood from a simple argument advanced in the next section. Figure 6(b) shows the variation of $V_{\max}$ with drop radius R for $\sigma = 0.001$. In contrast to the case of Fig. 6(a), no clear trend emerges from this, albeit limited, set of results and it seems possible that $V_{\max}$ is controlled in all but the smallest drops solely by local, microscopic considerations. Again this observed persistence of the microcurrent at all drop radii is in accordance with the simple argument advanced in the next section.

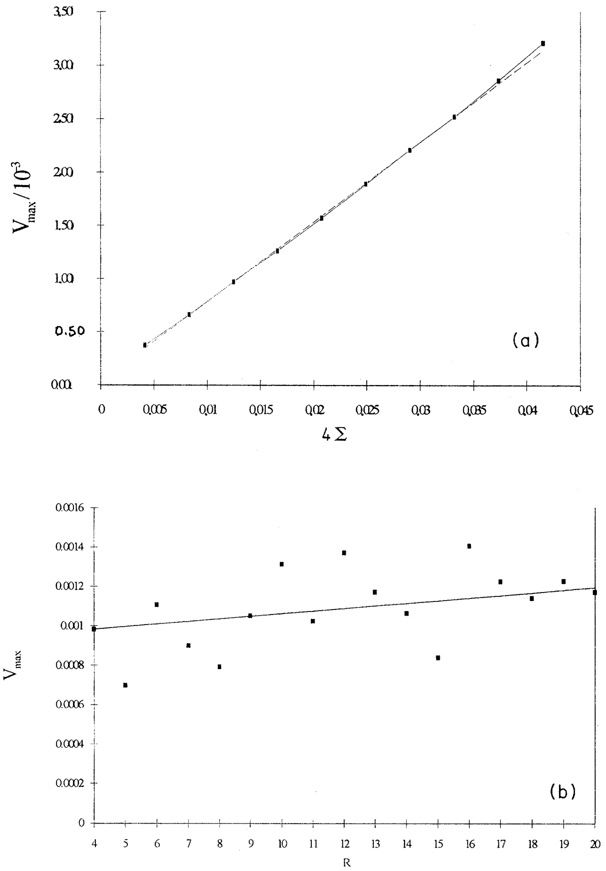

FIG. 6. (a) The maximum induced microcurrent velocity for a drop of radius 16 lattice units simulated using the hexagonal boundary conditions discussed towards the end of Sec. IV, recorded as a function of the simulation surface tension parameter Σ. The maximum velocities shown here were all recorded within a very small region of the lattice, close to the interface. Note the factor 4 attached to Σ on the horizontal axis. (b) Maximum microcurrent velocity shown as a function of drop radius R, for fixed σ. Data were obtained using the hexagonal boundary conditions discussed towards the end of Sec. IV. The solid line shows the least-squares fit. The absolute location of the site at which the maximum microcurrent velocity was found to occur of course varies with R. The location of this site *relative to the interface position* is—within the limits of our investigation—fairly constant for the drop radii recorded here.

All the lattice velocity fields produced in our simulations were constant between consecutive time steps and no *staggered momentum modes,* in which the velocity at a given site oscillates persistently between different stable values, were observed. Once the steady state is established the velocity field in both static and sheared drops is constant. During approach to the unsheared steady state, distinct whole-lattice velocity field configurations are observed near the drop. However, these modes decay and visual observation suggests, as one would expect, that restrictions of system geometry are responsible for the suppression of staggered momentum modes. It should be noted that red fluid pressure is observed initially to oscillate between one time step and the next, for a short period. In contrast, the plane boundary between static red and blue phases is unstable over long time scales. In this case two separate whole-lattice velocity field states arise and the simulation oscillates on alternate time steps between the two, for all time. Here staggered momentum modes dominate and no steady state arises.

Figures 7 and 8 represent a more quantitative comparison with theory. Figure 7 plots drop deformation against the parameter $\dot{\gamma}/\Sigma$ for the data used to compile Figs. 3 and 4. The linear correlation tends to imply that, over a range of both shear rates and surface tensions, and subject to the conditions set out below, D is governed by an equation such as (6.1) adapted for $k \gg \dot{\gamma}$ (low deformation), exhibiting correct functional dependence upon $\dot{\gamma}/\Sigma$.

The data presented in Fig 8 correspond to simulations of greater size (50×50) which can facilitate accurate measurement of small drop deformation and orientations away from 45°. Here we plot Cox's deformation D_C [Eq. (5.4) and [12]] against α, measured in radians, for the sake of small angle approximations. The different flow configurations observed were obtained by keeping the surface tension fixed and increasing the applied, far field

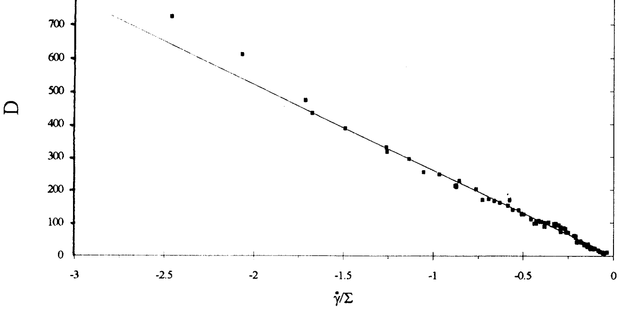

FIG. 7. Drop deformation as plotted against the parameter $\dot{\gamma}/\Sigma$ for all the data presented in Figs. 3 and 4. Quantitatively at least the expected trends are observed.

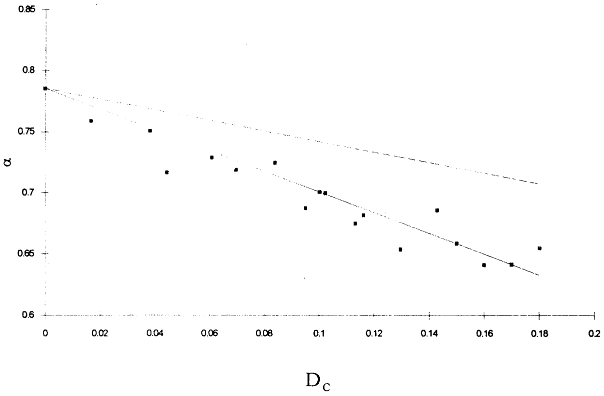

FIG. 8. The angular orientation of the drop, measured this time in radians, shown as a function of drop deformation measured by the parameter $D_C \equiv (a-b)/(a+b) \leq 0.2$ used in [12]. The range of D_C was determined so as not to exceed that of the results considered in [12]. The solid line corresponds to a least-squares fit to the data obtained from a drop of radius 10 units sheared on a lattice of 50×50. The ordinal intercept is $\pi/4$ rad and the gradient $-(0.847+0.157)$ rad. Theory predicts a gradient of -0.434 rad and an ordinal intercept of $\pi/4$ rad (broken line). The surface tension parameter σ in use was 0.001 which may be matched to a macroscopic (Laplace law) surface tension using Fig. 2.

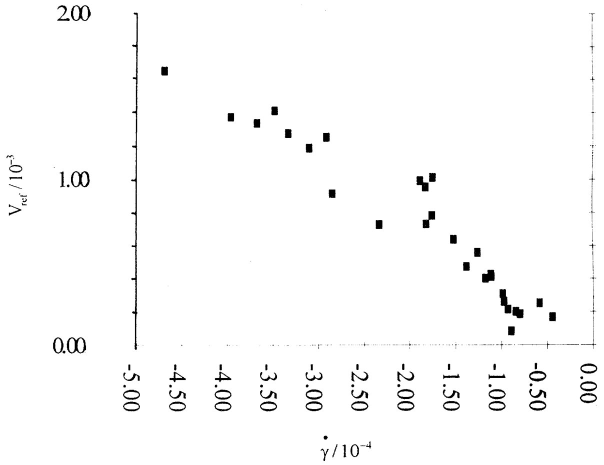

FIG. 9. The variation of a reference velocity, recorded at a distance of $1.6b$ along the projected semiminor axis (outside the drop) for the enlarged simulation sizes used for the results of Fig. 8. The forcing parameters in use produce velocities of a size similar to the microcurrent velocity—see Fig. 6.

shear rate over a restricted range ($\dot{\gamma} \leq 0.0005$ corresponding to $F_{\text{inc}} \leq 0.001$ and $\sigma = 0.001$). A restricted range of $\dot{\gamma}$ compared with that of Figs. 3 and 4 was necessary to limit the drop deformation and ensure compatibility with theory as discussed in Sec. V C. The macroscopic surface tension simulation parameter for these simulations may be inferred from Fig. 2.

A least-squares fit to this data (solid line, Fig. 8) gives an ordinal intercept of $\pi/4$ rad and a gradient of -0.847 rad with an error from convergence considerations of less than 18%. A careful check shows that the calculations of Cox appear to be valid when reduced to two dimensions. With some tedious but straightforward algebra, therefore, the (three-dimensional) perturbation calculations of [12] may be adapted to predict steady state drop deformation and orientations given (with our notation) by

$$D_C = \frac{5(19\lambda+16)\dot{\gamma}}{4(\lambda+1)\sqrt{(15k)^2+(19\lambda\dot{\gamma})^2}}, \tag{6.1}$$

$$\alpha = \frac{\pi}{4} - \frac{1}{2}\tan^{-1}\left[\frac{19\dot{\gamma}}{15k}\right], \tag{6.2}$$

where λ is the ratio of drop to suspending fluid shear viscosity. $k \equiv \Sigma/\eta V$ with V *a characteristic velocity in the region of the interface, relative to the center of the drop* [12]. It is the presence of the parameter V which restricts the extent to which the work of [12] may be used as the basis of quantitative comparisons. Note that the parameter $\dot{\gamma}$ appears explicitly in Eqs. (6.1) and (6.2) whereas it is set to unity in [12]. $\lambda = 1$ for our system and when $k \gg \dot{\gamma}$ (true for the situations of small deformation considered here) Eqs. (6.1) and (6.2) may be combined and one obtains, by using a small angle approximation, a relationship between D_C and α,

$$\alpha = \frac{\pi}{4} - \frac{76}{175}D_C, \tag{6.3}$$

in which α is measured in radians. This relationship is represented by the dashed line in Fig. 8, so that theory predicts that a plot of D_C against α should have a gradient of -0.434 rad and an ordinal intercept of $\pi/4$ rad. Considering static drops it was seen that lattice anisotropies are responsible for the relatively inferior fit at low deformation and deflection and it is this consideration alone which restricted the minimum measured angular deflection.

Figure 9 shows as a function of far field shear rate the variation in the velocity recorded at a distance of $1.6b$ along the projected semiminor axis (outside the drop) for the enlarged simulation sizes used in the results of Fig. 8. For the restricted range of shears employed ($\dot{\gamma} \leq 0.0005$) a typical flow velocity in the region of the interface is seen to be comparable with a typical microcurrent velocity (Fig. 6).

VII. DISCUSSION

Kingdon's nonlocal, nonlinear lattice Boltzmann algorithm, used in conjunction with the techniques of Gunstensen *et al.*, maintains a *locatable* and deformable interface. Moreover, the semiquantitative results in Figs. 3, 4, and 7 entail interfacial hydrodynamics with correct semiquantitative behavior. However, the results of Fig. 8 are a more stringent test of the model's interfacial hydrodynamics, from which a certain need for more detailed comparisons with theory is seen to arise. Figure 8 shows that drop deformation D_C is smaller than theory predicts by some 50%, for a particular value of α, which highlights a need for direct measurements of interfacial boundary conditions. However, the ordinal intercept in Fig. 8 and the functional relationship between D_C and α are in good agreement with theory.

Additional to the continuity of velocity components through the interface, hydrodynamic boundary conditions require tangential and normal contractions of stress [7] to satisfy (in two dimensions)

$$n_k \sigma_{ik}^{\text{red}} - n_k \sigma_{ik}^{\text{blue}} = \frac{\Sigma}{R} n_i \ , \tag{7.1}$$

$$t_k \sigma_{ik}^{\text{red}} - t_k \sigma_{ik}^{\text{blue}} = 0 \ , \tag{7.2}$$

where σ_{ik}^{red} and $\sigma_{ik}^{\text{blue}}$ denote the red and blue fluid stress (defined in [4]), R the local interfacial radius of curvature and $n_k(t_k)$ components of the local interface normal (tangent), all of which may be measured from simulations. In this way conditions (7.1) and (7.2) may be assessed directly. Figure 6, which, after Gunstensen [5], catalogues microcurrent activity in the region of the interface in a *static* CA fluid raises obvious questions in respect the extent that Eqs. (7.1) and (7.2) will represent the LBILG interfacial hydrodynamics. It is possible that the microcurrent is responsible for the reduced deformation at given α recorded in Fig. 8 by insulating the drop interior. Indeed, typical microcurrent velocities (Fig. 6 and [5]) are of a size with those induced by the external flow, close the interface. Increasing shear rate can no more illuminate the influence of the microcurrent (by rendering it *pro rata* less significant) using our methods, however, for the ensuing increased deformation lies outside the range of the theoretical predictions of [12]. However the results presented in Figs. 3, 4, and 7 (in which D, *not* Cox's D_c, features) when so arranged show a constant linear relationship between α and D persisting up to much higher shear rates, where microcurrent activity may be expected to be less. But that flow stresses *are* transmitted in a manner which is substantially correct appears, from our results, likely.

Although the microcurrent might be reduced, for example, by incorporating a factor in the right-hand side (RHS) of (3.3) which decreases the surface tension perturbation for sites with increasing color purity, a microcurrent-free LBILG, whilst desirable, would be, on the following simple argument, an unattainable solution for any lattice gas relying upon a segregation rule as the source of interfacial tension. Consider a lattice site adjacent to a mixed site in an established interface with a large radius of curvature. Segregation of colored species at the mixed site (after Gunstensen) necessarily generates *perturbed* densities, which propagate onto the bulk site considered, where links with a component along the local color field direction will therefore contain larger-than-average incoming densities (from the interfacial site). The constraint of momentum conservation in subsequent collision processes will preserve this momentum anisotropy, which as a result will propagate further away from the interface. The parameter σ controls the extent of this effect proportionately through the magnitude of density perturbations manufactured in the interface [see (3.3)]. On this argument one expects principal microcurrent velocities to be proportional to σ—in agreement with observations. We should expect a microcurrent generated in this way to have a limited extent for the concentration of perturbed densities will decline away from the interface, which appears to be the case in our results. In a local average of momentum over a group of sites located around (on both sides of) an interface the microcurrent, from a few obvious tests, was observed to average to zero, which restricts the extent to which microcurrents actually advect momentum.

Perturbation (3.3) has been used in this work for inserting anisotropy into the pressure tensor (2.3) and hence for the value of macroscopic surface tension. Gunstensen *et al.* have remarked that (3.3) is phenomenological: as such any perturbation with the same properties [3] is a possible alternative. The density perturbation produced by the RK rule in a CA may be measured or calculated and regarded as the most authentic possibility. However, a closed, analytical expression for the ensemble averaged *automaton* interfacial density perturbation is unknown to the authors and any measurement would still have to be approximated for efficient application in a LBILG. Nevertheless, the analytical form of the density perturbation induced in Rothman-Keller automaton interfaces remains an interesting question.

VIII. CONCLUSIONS

Combining Kingdon's particular lattice Boltzmann scheme with Gunstensen's technique we have produced a LBILG with an interface which is *locatable* for the purpose of assessing the hydrodynamics of the interface. Rothman and Keller previously showed that a static suspended drop exhibits behavior consistent with Laplace's law and our LBILG also exhibits this behavior.

Our results for the steady state dynamics of two immiscible lattice Boltzmann fluids demonstrate that, with the effective surface tension controlled by a parameter of the model, a suspended drop deforms in a shear flow with the expected functional dependence upon applied, far field shear rate and surface tension. The deformed drop orientation is also observed to have qualitatively correct behavior. The quantitative relationship between the angle α and the deformation D_C is unfortunately less encouraging, the measured gradient from Fig. 8 being $-(0.847\pm0.152)$ rad against a theoretical value of 0.434. The predicted and measured ordinal intercepts are in very close agreement, however.

Mesoscopic interfacial microcurrents apparently allow the transmission of shear stresses over the range of simulation parameters and, in this work, that range was determined from considerations of system size. Whilst characteristic microcurrent velocities encountered are not small compared to those induced close to the interface by the externally applied flow field, velocity and stress transmission across the interface are clearly observed and in part "correct." Yet it may be that at small induced shears this no longer remains true, but this will prove difficult to establish, without rather large simulations. Increasing shear rate can no farther illuminate the influence of the microcurrent using our methods, for the ensuing increased deformation lies outside the theoretical predictions employed. The best hope for further work lies in large shear rate direct measurement of stress contractions. However, the work to date suggests that the microcurrents do not, we believe, severely limit the applicability of the method.

Questions remain to be addressed. Comparisons with results correct for large shear rates and drop deformation or direct measurement of the interfacial stress contractions in this regime perhaps offer the best way forward towards a fuller appreciation of LBILG interfacial hydrodynamics. Then there are many potential applications of the method to problems in multiphase fluid flow alone.

---

[1] U. Frisch, D. d'Humieres, B. Hasslacher, P. Lallemand, Y. Pomeau, and J. P. Rivet, Complex Syst. **1**, 649 (1987).

[2] D. H. Rothman and J. M. Keller, J. Stat. Phys. **52**, 1119 (1988).

[3] A. K. Gunstensen, D. H. Rothman, S. Zaleski, and G. Zanetti, Phys. Rev. A **43**, 4320 (1991).

[4] R. Kingdon, J. Phys. A **25**, 3559 (1992).

[5] A. K. Gunstensen, Ph.D. thesis, MIT, 1992, p. 48.

[6] J. Armstrong (unpublished).

[7] L. D. Landau and E. M. Lifshitz, *Fluid Mechanics,* Course of Theoretical Physics Vol. 6 (Pergamon, Oxford, 1966).

[8] F. J. Higuera and J. Jiminez, Europhys. Lett. **9**, 663 (1989).

[9] S. Wolfram, J. Stat. Phys. **45**, 471 (1986).

[10] R. Kingdon (private communication).

[11] H. Goldstein, *Classical Mehcanics,* 9th ed. (Addison-Wesley, Reading, MA, 1966).

[12] R. G. Cox, J. Fluid Mech. **37**, 601 (1969).

[13] G. K. Batchelor, *An Introduction to Fluid Dynamics* (Cambridge University Press, Cambridge, England, 1967).

[14] H. Lamb, *Hydrodynamics,* 6th ed. (Cambridge University Press, Cambridge, England, 1932).

[15] G. I. Taylor, Proc. R. Soc. London Ser. A **138**, 41 (1932).